Size- and temperature-dependent epitaxy for a strong film-substrate mismatch: The case of Pt/MgO(001)

J. Olander, R. Lazzari,* J. Jupille,† B. Mangili, and J. Goniakowski‡
Institut des NanoSciences de Paris, CNRS UMR 7588-Universités Pierre et Marie Curie (Paris 6) et Denis Diderot (Paris 7), Campus Boucicaut, 140 Rue de Lourmel, 75015 Paris, France

G. Renaud§
CEA-Grenoble, Département de Recherche Fondamentale sur la Matière Condensée, Service de Physique des Matériaux et Microstructures, Nanostructures et Rayonnement Synchrotron, 17 Avenue des Martyrs, F-38054 Grenoble, Cedex 9, France
(Received 14 March 2007; revised manuscript received 21 May 2007; published 7 August 2007)

The growth of platinum film on MgO(001) was analyzed in a combined experimental and theoretical study. Experiments were performed by grazing-incidence x-ray diffraction at small [grazing-incidence small-angle x-ray scattering (GISAXS)] and wide [grazing-incidence x-ray scattering (GIXS)] angles, and the theory coupled *ab initio* calculations on model Pt/MgO(001) systems and large-scale simulations of supported Pt clusters using a coordination-dependent interaction potential. GISAXS data showed that the cluster aspect ratio is constant at all studied temperatures with a tendency to faceting at 1000 K. The cluster spacing at the early stage of the growth is characteristic of a growth on defects, while the particle size obeys a $d \sim t^{0.5}$ power law assigned to dynamic coalescence. All Pt films deposited at 1000 K show the $[100](001)_{Pt} \| [100](001)_{MgO}$ epitaxy. As the cluster size increases, the in-plane Pt-Pt distance increases above the bulk value (0.393 nm), passes through a maximum (0.398 nm) at a thickness of $t=0.6$ nm, and then relaxes back to the bulk value through interfacial dislocations, a behavior predicted by calculation and which appears typical of (001) epitaxy. Finally, the formation of dislocations arising from the Pt/MgO(001) mismatch of −6.83% is evidenced. Below 1000 K, due to a minimization of the surface energy of the film, the $(111)_{Pt} \| (001)_{MgO}$ epitaxy dominates. Beside the expected $[1\bar{1}0](111)_{Pt} \| [110](001)_{MgO}$ orientation, another epitaxy is revealed, i.e., $[1\bar{1}0] \times (111)_{Pt} \| [100](001)_{MgO}$. Moreover, families of orientations slightly rotated relative to the former epitaxy are evidenced. Calculations reveal that intermediate minima in energy appear at angles that depend on the size of the particles. Comparison between Ni/, Pd/, Pt/, and Ag/MgO(001) shows that the progressive weakening of the metal-MgO bonding in this order explains the decrease in adhesion energy as well as in metal-MgO distance, which are experimentally and/or theoretically observed through that series.

DOI: 10.1103/PhysRevB.76.075409 PACS number(s): 81.15.Aa, 61.10.−i, 68.55.−a

I. INTRODUCTION

The nonreactive Ag/, Pd/, and Pt/MgO(001) systems are test beds for the fundamental issues regarding the contact between dissimilar materials,[1–5] because they offer favorable conditions for both experimental and theoretical investigations. Indeed, a weak charge transfer results in abrupt interfaces, while the checker board ordering of the equivalent cation and anion sites of the MgO(001) cleavage plane facilitates the structural analysis. The cubic structure and the lack of strong electronic correlations in MgO make calculations more tractable. Moreover, these systems have been thoroughly investigated as model catalysts.[3,5] Among them, the Ag/ and Pd/MgO(001) interfaces are today close to a consensus in every respect. X-ray absorption and x-ray diffraction experiments have demonstrated that silver[6–8] and palladium[9] adatoms prefer to sit atop surface oxygen atoms, in agreement with theory.[10–12] Moreover, such behavior is now predicted over all transition-metal series.[13,14] On MgO(001), the face-centered-cubic (fcc) Ag and Pd grow in the so-called cube-on-cube $[100](001)_{Metal} \| [100](001)_{MgO}$ (Refs. 8 and 9) epitaxial orientation. Despite an interface lattice parameter mismatch of −7.64%, Pd forms pseudomorphic films on MgO(001).[9] With a lattice mismatch of −3%, the weakly bonded Ag/MgO(001) interface is never pseudomorphic,[8] although the Ag-Ag distance undergoes a significant expansion.[8,15] Cluster shapes and dislocation networks have also been investigated in both systems.[4,9] The truncated Pd octahedra formed on MgO(001) were interpreted in the framework of the Wulff-Kaishew theory.[16–20] Strain release at the Ag/MgO(001) interface results in dislocations oriented in the ⟨110⟩ direction,[4,8] which were used as a template to grow organized particles[21] via a favorable adsorption on the tensile surface regions.[22]

At variance with these systems, the Pt/MgO(001) interface is far from being understood. Indeed, the much debated question of the epitaxial orientation of platinum on MgO(001) is of relevance in a variety of topic areas. The high melting temperature and the stability against corrosion of platinum make it suitable for buffer layers and electrodes[23,24] in devices for optical, magnetic, and magneto-optic applications. As a known catalyst for dehydrogenation and low temperature combustion, platinum acquires some specific properties with respect to alkane conversion[25,26] and combustion of methanol[27] if supported on the very basic MgO. These applications have prompted the use of various methods to grow platinum films on the MgO(001) surface, including pulsed laser deposition,[24,28–30] electron beam evaporation,[31–33] and sputtering.[23,34–36]

The occurrence of a chemical reaction at the Pt/MgO(001) interface is unlikely because of the small electronegativity of platinum. However, a very strong interfacial bonding is predicted.[37] The Pt/MgO mismatch amounts to $(a_{Pt}-a_{MgO})/a_{MgO}=-6.83\%$ ($a_{MgO}=0.42119$ nm and $a_{Pt}=0.39242$ nm). The Pt/MgO(001) films grow in the Volmer-Weber mode. Two epitaxial orientations are commonly found, $[100](001)_{Pt}\|[100](001)_{MgO}$ and $[1\bar{1}0](111)_{Pt}\|[110]\times(001)_{MgO}$,[28,38,39] which compare with the low energy interfaces listed by Fecht and Gleiter[40,41] for gold on MgO(001). As a general trend, these two orientations coexist at low temperature, while the cube-on-cube Pt(001) orientation is favored under conditions of low supersaturation[32] and tends to dominate films deposited at higher temperature. This can be simply explained by a competition between the lowest surface energy $(111)_{Pt}$ and the most favorable interfacial orientation $(001)_{Pt}\|(001)_{MgO}$.[42] The flux and energy of the deposited species also play a role in the orientation and crystallinity of the film.[23,24,30] Pure cube-on-cube $(001)_{Pt}$ orientation is produced (i) at 570 K by laser ablation in the presence of a partial pressure of oxygen higher than 10^{-4} mbar and (ii) at a temperature as low as 370 K by triode sputtering with an argon pressure that is much reduced (4×10^{-4} mbar) with respect to the usual processing conditions.[23] The cube-on-cube orientation is dominant in films obtained by pulsed laser deposition above 770 K.[30] However, there is still some $(111)_{Pt}$ within films deposited at 950 K by magnetron sputtering.[35] The $(001)_{Pt}$ orientation is also observed by annealing of implanted platinum in MgO.[43] The dependence of the epitaxy of the platinum film upon incoming flux, substrate temperature, and deposition technique indicates that kinetics plays a central role in the observed complexity of the Pt/MgO(001) interface. The equilibrium situation is not clear either. Indeed, the orientation of the Pt/MgO(001) layer, which is partly a consequence of competition between the surface and interface energies, depends on the film thickness. The $(111)_{Pt}$ orientation is increasingly prevalent with increasing thickness.[31,32,34] As an example, a 4 nm thick Pt film deposited by electron beam evaporation on MgO(001) at 970 K is almost completely (001) oriented. In contrast, the (200)/(111) Bragg reflection ratio in a film of ~30 nm is approximately 1:2.[32]

To date, most studies of the Pt/MgO(001) system have been performed *ex situ*, and a comprehensive *in situ* study of the system during its growth is still lacking. The aim of the present work is to clarify these epitaxial relationship issues, in a combined experimental and theoretical approach, making the link with both the morphology of the deposit and the way the lattice parameter mismatch is released at the interface. The experimental study is performed *in situ* during the first stages of the growth of Pt on MgO(001) by physical evaporation. The experimental part combines *in situ* grazing-incidence small-angle x-ray scattering (GISAXS),[44] which provides information on the shape, size, and organization of the growing deposit, with *ex situ* and *in situ* grazing-incidence x-ray scattering (GIXS),[45] which provides structural information at the atomic level. Calculations were performed on different levels of complexity. To analyze the nature and to quantify the interaction between Pt and the MgO(001) surface, a series of Pt-MgO interfaces has been modeled at the *ab initio* level. On this basis, a large-scale semiempirical simulation of supported Pt clusters has been performed. The behavior of the equilibrium cluster shape and atomic structure as a function of cluster size will be used to rationalize the experimental results.

II. METHODS

A. Experimental setups of grazing-incidence x-ray scattering

The GIXS experiments were performed on two different surface diffractometers (GMT and SUV) of the BM32 bending magnet beamline (Collaborating Research Group/Interfaces)[46] at the European Synchrotron Radiation Facility (ESRF), Grenoble, France. The SUV setup combines a large surface diffractometer with a large epitaxial chamber equipped with Be windows to let the x-ray beam enter and exit. It allows both GIXS and GISAXS measurements *in situ* during Pt deposition in ultrahigh vacuum (UHV) conditions (base pressure of 10^{-10} mbar).[47,48] The GMT diffractometer, equipped with a secondary vacuum chamber in which the samples can be annealed, was used for the *ex situ* measurements. While samples studied with SUV were grown *in situ*, during the measurements, those studied in GMT, called *ex situ* samples, were produced in another UHV chamber. GISAXS data were collected on both the ID32 undulator beamline (ESRF) and the BM32 beamline. The ID32 setup was designed without any beryllium window between the storage ring and the sample to avoid background scattering.[16] On the BM32 beamline, GISAXS was performed in the SUV setup equipped with motorized vacuum beam stop (to stop the specular and direct beams) and guard slits (to avoid background scattering from Be windows).[20,48] The distance between the x-ray charge-coupled device detector and the sample was set to 1.010 m on ID32 and 0.610 m on BM32, pixels corresponding to 66.84×66.84 μm^2 and 56.25×56.25 μm^2, respectively.

On both SUV and GMT setups, the monochromatic x-ray beam was focused both horizontally (H) and vertically (V), with a full width half maximum (FWHM) of 0.4 mm (H) $\times$0.3 mm (V) and a divergence of 1 mrad (H) $\times$0.13 mrad (V), and further defined by a set of entrance slits. It is shone on the vertical sample surface under a grazing incidence α_i. The signal scattered at wide angles is collected on a NaI scintillator detector in a direction defined by two sets of vertical and horizontal slits, with typical angular acceptances between 1 and 3 mrad. When using an x-ray beam energy of 18.5 (11) keV, the critical angles for total external reflection α_c of MgO and Pt are 0.12° (0.20°) and 0.29° (0.49°), respectively. Also available are the complex index of refraction[49] $n=1-\delta-i\beta$ at the two energies used: $\delta_{MgO}=2.28\times10^{-6}$ (6.13×10^{-6}), $\beta_{MgO}=4.96\times10^{-9}$ (3.52×10^{-8}) and $\delta_{Pt}=1.07\times10^{-5}$ (2.63×10^{-5}), $\beta_{Pt}=1.15\times10^{-6}$ (1.64×10^{-6}). Incident angles close to the MgO critical angle were used to minimize the background arising from Compton scattering and from point defects in the bulk.

The samples are flat MgO(001) surfaces of high crystallinity, prepared in a way described previously,[50] with an in-

TABLE I. The experimental parameters for each sample studied by GISAXS or GIXS, specifying the deposition conditions (*In situ* or *ex situ* experiment), deposition temperature T_{dep}, growth rate and/or film thickness t, annealing temperature T_a, the x-ray beam parameters (incident angle α_i and energy E), and the instrument used (GMT or SUV).

Expt.	Name	Growth	T_{dep} (K)	t (nm)	T_a (K)	α_i (deg)	E (keV)	Instrument
GISAXS	S1-00	*In situ*	1000	0.8/h	No	0.2	11	ID32
	S2-00	*In situ*	800	0.6/h	No	0.2	11	ID32
	S3-00	*In situ*	600	0.4/h	No	0.2	11	BM32-SUV
GIXS	S1-98	*Ex situ*	800	3.5	No	0.6/0.14	11/18.5	BM32-GMT
	S2-98	*Ex situ*	300	19.5	1500	0.1	18.5	BM32-GMT
	S3-98	*Ex situ*	200	6.0	1600	0.12-0.5	20	BM32-GMT
	S1-99	*In situ*	1000	0–2.5	No	0.1	18	BM32-SUV
	S2-99	*In situ*	1000	0–6.5	No	0.12	18	BM32-SUV

plane domain size of 1 μm and an average terrace size of 600 nm. The surface cleanliness was checked by Auger spectroscopy. Pt films were produced by electron beam evaporation (Omicron NanoTechnology EFM4, Germany) of a Pt metal rod (2 mm diameter, 99.99% purity). The substrate temperature was kept constant during deposition. The Pt deposition rate was measured with a quartz microbalance and cross-checked afterward by x-ray reflectivity. The growth conditions are presented in Table I. The *in situ* GIXS and GISAXS measurements were generally performed on Pt films grown step by step, the growth being interrupted during data acquisition. However, the ID32 GISAXS experiments on samples S1-00 and S2-00 were performed upon a continuous Pt flux.

The Miller indices $(hk\ell)$ were generally expressed in reciprocal lattice units (rlu) of MgO by referring to the bulk parameter ($a_{\mathrm{MgO}}=0.421\ 19$ nm). The few cases where Pt rlu were used are indicated. In all cases, the ℓ index is related to the component of the wave vector transfer perpendicular to the surface.

B. Computational method: Model of interactions and search of cluster equilibrium shape

Our energetic approach couples the well-established second moment approximation (SMA) potential for metal-metal interactions within the cluster with a many-body potential energy surface (PES) representing the metal-MgO interaction. Quenched molecular dynamics is used to determine the precise equilibrium atomic structure of supported clusters.

In the SMA,[51] the attractive part of the potential is fitted to the band energy, assuming a rectangular density of states of the same width as the actual one. In the form proposed by Rosato *et al.*,[52] this attractive term is supplemented with a phenomenological core-repulsion term of the Born-Mayer type. Full details on this implementation of the SMA potential, together with the particular set of parameters for Pt, have been given in Refs. 53 and 54. It has been already used in a study of structural transitions in icosahedral, decahedral, and octahedral free Pt nanoclusters.[53] Its validation against density functional theory (DFT) results on Pt nanoclusters has also been discussed.[55] We remind that this parametrization of the SMA results in a systematic underestimation of the surface energies σ. In the particular case of Pt, the SMA estimate $\sigma_{(111)}=1.01\ \mathrm{J/m^2}$ is more than twice smaller than the corresponding *ab initio* (2.69 $\mathrm{J/m^2}$, Ref. 56) and experimental (2.56 $\mathrm{J/m^2}$, Refs. 57 and 58) values. The effect of this underestimation on the calculated equilibrium shape of the supported particles will be discussed in the paper. However, the anisotropy factor $\sigma_{(001)}/\sigma_{(111)}$, the second parameter which drives the shape of particles, is reproduced fairly well. Our calculated value of 1.14 approaches very closely the recent *ab initio* estimation of 1.17.[56]

The effective metal-MgO interaction was constructed and parametrized in a way analogous to that of our earlier works on Pd/MgO(001), Ag/MgO(001), and Ni/MgO(001) interfaces.[19,22,59–61] Namely, the metal-MgO interaction was assumed additive with respect to metal atoms, but dependent on their coordination. The nonlinear dependence of the interaction energy on the metal coordination is particularly important in systems with a large proportion of undercoordinated atoms (small clusters) and it confers to the fitted PES an effective many-body character. In the case of Pt-MgO, the analytical form of the interaction was adjusted to the results of DFT calculation on the generalized gradient approximation[62] level performed with the Vienna *ab initio* simulation package[63] on a series of model systems, including three different metal adsorption sites (oxygen, magnesium, and hollow) and at three different metal coverages [0.25, 1.0, and 5.0 ML (monolayer)]. Intermediate cases (with respect to both the adsorption site and the metal coverage) were obtained by interpolation. The set of parameters representing the Pt-MgO(100) PES is listed in Ref. 64. In the DFT calculations, we have imposed a (2×2) (1/4 ML) or (1×1) (1 and 5 ML) interface unit cell with MgO lattice parameters. The MgO(001) substrate was modeled by a three-layer-thick slab. All atoms of the Pt deposits and both surface and subsurface MgO layers have been fully relaxed. The third MgO layer has been kept fixed and was taken as a reference in estimations of interface distance d_{int}. The separation energy has been calculated with respect to the clean MgO(001) sur-

TABLE II. Interface separation energy E_{sep} (eV) and interface distance d_{int} (nm) as obtained for model Pt-MgO(001) interfaces corresponding to different metal coverages (0.25, 1.0, and 5.0 ML) and to different adsorption sites (oxygen and magnesium).

	1/4 ML		1 ML		5 ML	
	O site	Mg site	O site	Mg site	O site	Mg site
E_{sep} (eV)	2.50	0.70	0.44	0.14	0.40	0.14
d_{int} (nm)	0.19	0.248	0.227	0.302	0.243	0.313

face and to the unsupported, relaxed Pt film. The main results of these calculations are summarized in Table II. As in the case of Pd/MgO(001) interface, we find that, regardless the metal coverage, the sites on top of substrate oxygen are by far energetically the most favorable, while magnesium and hollow sites represent minima and saddle points of the PES. Interface distances vary accordingly. The interaction strength decreases progressively as the metal coverage increases, revealing an important contribution of the Pt-O chemical bonding. We note a particularly strong metal-MgO interaction at the lowest coverage (isolated atoms). This effect has already been reported in the past and attributed to a specific structure of the Pt valence band.[11] Our computational data for the lowest Pt coverage agree well with the results by Bogicevic and Jennison,[65] but we obtain a somewhat stronger Pt-MgO bonding than that reported by Grönbeck and Broqvist.[37]

Following the present experimental evidence, we focus on truncated octahedral clusters only. Indeed, while the very same energetic model predicts truncated decahedral shape for free Pt nanoclusters of similar sizes,[53,66] we note that a strong substrate-induced reduction of the critical size for the structural transition between decahedrons and octahedrons has been explicitly evidenced in the similar case of MgO(100)-supported Pd nanoclusters.[67] In order to consider complete families of truncated octahedral clusters in Pt(111) and Pt(001) epitaxy, rather than to perform a global structural optimization (e.g., by cycles of cluster melting and recrystallization[67,68]), we have chosen to proceed by a local geometry optimization for each epitaxy with a large variety of initial cluster forms. The latter were obtained systematically by truncations of a bulk Pt crystal, corresponding to various Wulff polyhedrons[69] and exposing different proportions of (111) and (001) facets. Upon the deposition on the MgO(001) surface, these polyhedrons were further truncated, in the spirit of the Wulff-Kaishew construction.[70] Except the smallest clusters, which will be not considered here, the above procedure preserves the initial face-centered-cubic structure of the metal and its initial epitaxy relation with the substrate. Thus, it enables the construction of the two distinct families of deposited Pt clusters.

III. GROWTH MODES AND COMPLEX EPITAXIES AT THE PT/MgO(001) INTERFACE

A. Coalescence of platinum on MgO(001)

GISAXS patterns of supported particles involve two broad scattering lobes (Fig. 1) that show up on each side of the specular rod. The extension of the scattering parallel (perpendicular) to the surface is inversely proportional to the average particle in-plane diameter d (height H), and the separation between the two lobes is inversely proportional to the average distance D between neighboring particles. The patterns observed herein are consistent with the expected Volmer-Weber growth mode of Pt/MgO(001). As an example of the data evolution during growth, Fig. 2 shows two cuts (parallel and perpendicular to the surface) of the GISAXS intensity maps for successive deposits at 600 K. As all direct space parameters increase upon the film growth, the lobes shrink and shift toward the center of the reciprocal

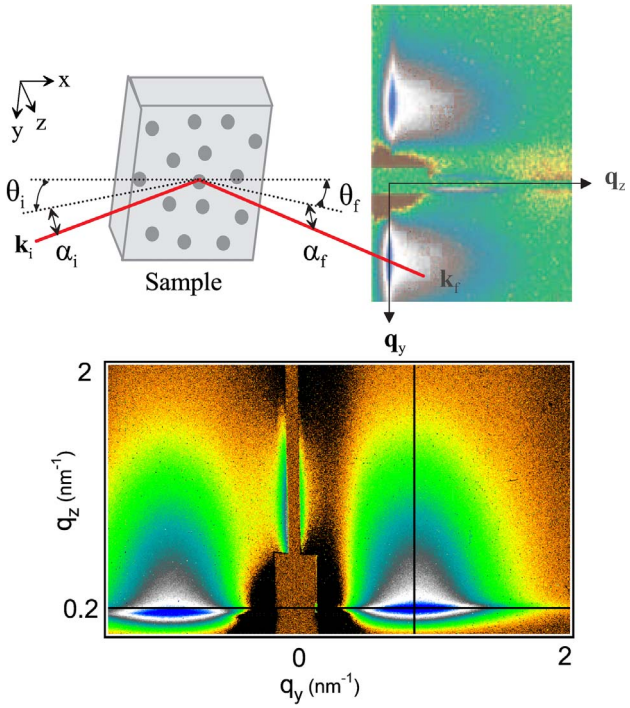

FIG. 1. (Color online) (a) During GISAXS experiments, the incident x-ray beam (wave vector $\mathbf{k}_i$) impinges on the sample surface under a grazing incidence α_i. The scattered intensity is recorded in the far field region as a function of the out-of-plane angle α_f and the in-plane angle $2\theta_f$. The wave vector transfer is denoted by $\mathbf{q}=\mathbf{k}_f-\mathbf{k}_i$, where $q_x=k_0[\cos(\alpha_f)\cos(2\theta_f)-\cos(\alpha_i)]$, $q_y=k_0[\cos(\alpha_f)\sin(2\theta_f)]$, and $q_z=k_0[\sin(\alpha_f)+\sin(\alpha_i)]$ with $k_0=2\pi/\lambda$, λ being the x-ray wavelength. (b) A typical experimental GISAXS pattern of Pt deposited on MgO(001), with two scattering lobes in the (q_y,q_z) plane. The two characteristic line cuts used in the fitting procedure are shown as thick-line.

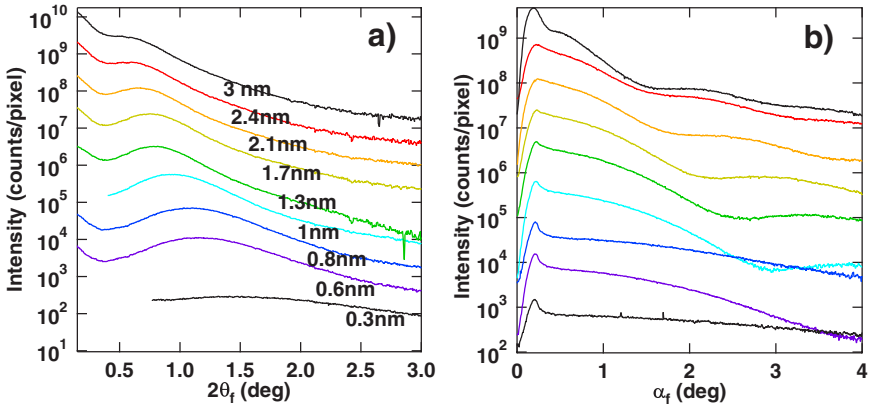

FIG. 2. (Color online) GISAXS data collected during the growth of Pt on MgO(001) at 600 K for deposits from 0.3 to 3 nm. (a) The intensity in the direction parallel to the surface $q_y \sim 2\theta_f$ at the location of the refraction peak. (b) The intensity in the direction perpendicular to the surface $q_z \sim \alpha_f$ at the location of the correlation peak maximum. A y offset for each curve was applied for clarity. Notice the progressive shift for the Yoneda's peak from the refraction on the bulk MgO to refraction on Pt.

space. In the direction perpendicular to the surface, the position of the intensity maximum, called Yoneda's peak, which is expected to correspond to the critical angle of the effective surface, is observed to shift from the critical angle α_c of MgO to that of Pt upon increasing thickness. In addition, as a result of the increase in the particle height, interference fringes progressively appear perpendicular to the surface and get sharper and sharper and their period shortens.

The experimental GISAXS data were quantitatively analyzed by means of the ISGISAXS program[71,72] using the distorted wave Born approximation[73] and local monodisperse approximation[20,74] formalisms. The one-dimensional paracrystal[75] with Gaussian statistics was chosen to account for the interference between scatterers. The size distributions parallel and perpendicular to the substrate were modeled by uncoupled Gaussian laws. Two cross sections (Fig. 3) along q_y and q_z at the maximum of scattered intensity, i.e., at the positions of the correlation and Yoneda's peaks, respectively (Fig. 1), were simultaneously fitted using a Levenberg-Marquadt χ^2 minimization. To improve statistics, additional profiles collected farther away in the reciprocal space were also fitted. Scattering patterns from Pt/MgO(001) films deposited at 600, 800, and 1000 K (see Table I) were analyzed at several thicknesses.

Films grown at 600 K (Figs. 2 and 3) and 800 K were simply fitted by means of truncated sphere shapes. Indeed, the GISAXS intensity maps did not show any anisotropy upon rotating the sample, nor any scattering rod characteristic of oriented facets, and the behavior of the intensity at high wave vector transfer[20] ("Porod's regime") was characteristic of such a shape. The quality of the model was judged by the way it reproduced the intensity profiles [Figs. 3(c) and

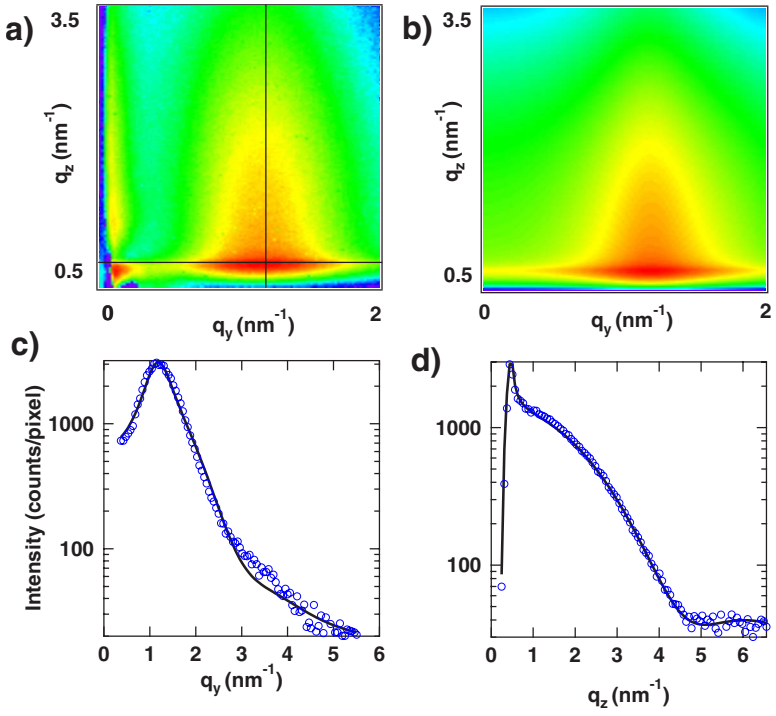

FIG. 3. (Color online) 2D GISAXS patterns for a 0.3 nm thick deposit at 600 K. (a) Experimental 2D pattern and (b) GISAXS pattern simulated with the parameters obtained from the fits made along the (c) parallel and (d) perpendicular linear cuts through the intensity maximum (shown in *a* map). In (c) and (d), the continuous lines correspond to the best fits and the dots to data points. Images are plotted on a logarithmic color scale.

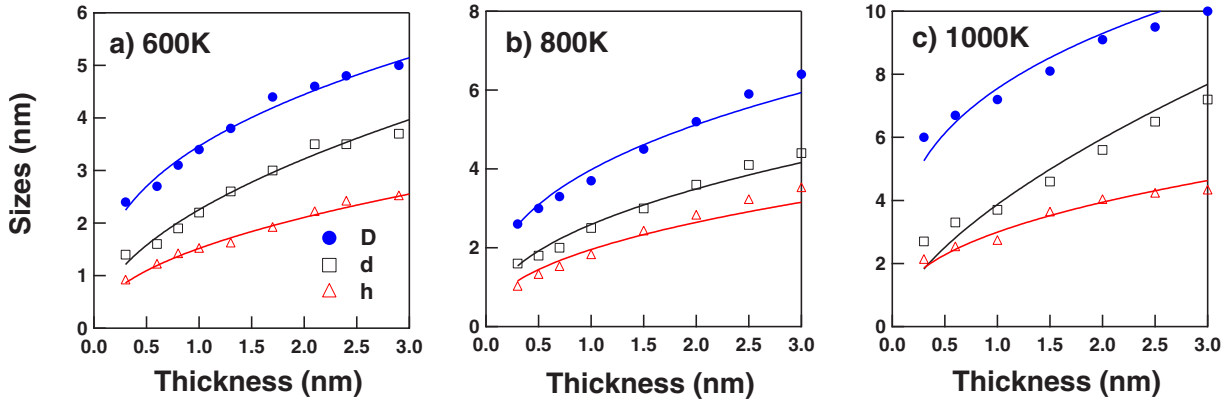

FIG. 4. (Color online) Results deduced from a full GISAXS analysis of the data for deposits made at (a) 600 K, (b) 800 K, and (c) 1000 K (see text for details). The evolutions of island spacing D (solid circles), mean lateral size d (open squares), and mean height H (open triangles) with increasing Pt thickness are shown with the power law fitted continuous line.

3(d)], and the two-dimensional (2D) GISAXS pattern [Fig. 3(b)]. However, models based on cylindrical and spherical particle shapes failed in the case of films deposited at 1000 K. Good fits were instead obtained only by representing clusters by a truncated pyramid with a square basis. The fitted angle of the side facets corresponds to islands that display (111) planes in cube-on-cube $(001)_{MgO}\|(001)_{Pt}$ epitaxy. Consistently, diffuse scattering rods inclined at 54.7° (Ref. 16) were observed on some GISAXS images.

The evolution with deposited thickness of the obtained morphological parameters (diameter, height, and interisland distance) are presented in Fig. 4 for three growth temperatures (600, 800, and 1000 K). A comparison between the mean film thickness calculated from these latter and the expected one shows that the sticking coefficient of Pt/MgO(001) is between 0.35 and 0.55 at the studied temperatures. At the smallest coverage of 0.3 nm, the interisland distance is around 2.5 nm at 600 and 800 K, which is characteristic of nucleation on defects because the corresponding density of particles is very high ($\rho \sim 1/D^2 = 1.6 \times 10^{13}$ cm^{-2}) and does not depend on temperature. However, for the same coverage at 1000 K, $D=6$ nm is two times higher probably because of a temperature-enhanced detrapping of atoms from defect sites and an increase of the critical nucleus size needed to avoid dissolution.

The particle aspect ratio H/d is close to the constant value of 0.7 (Fig. 5), whatever the growth temperature or the amount of deposited material. Together with the faceting observed for the particle grown at 1000 K, this indicates that particles get close to their equilibrium shape. The continuous increase of interisland distance D (Fig. 4) evidences that coalescence occurs all along the deposition and that the nucleation-growth step happens before the start of the GISAXS measurements, i.e., before 0.25 nm thickness. Data points at all temperatures can be represented by power laws with evaporation time, i.e., $d \sim t^{0.5}$ and $D \sim t^{0.3}$, respectively (Fig. 4). The coalescence mechanism may involve the static meeting of particle growing at fixed position or a dynamic diffusion of clusters. If the reshaping of particles is faster than the time scale of impinging atoms, analytical models, scaling descriptions, and numerical simulations[76–78] of static coalescence agree on a $d \sim t^1$ power law behavior. Power laws relative to the spacing between clusters are more scattered: $D \sim t^1$ (Refs. 76 and 77), $D \sim t^{0.135}$ (Refs. 79 and 80) for homogeneous nucleation, and $D \sim t^{0.5}$ (Ref. 80) for heterogeneous nucleation. The discrepancy with the actual measurement on the diameter d rules out the static mechanism. Instead, the actual $d \sim t^{0.5}$ and $D \sim t^{0.3}$ laws are close to that derived for dynamic coalescence in breath figures[81] in a case in which the diffusion of droplets leads to a bimodal size distribution where the biggest particles follow $d \sim t^{0.48}$ and $D \sim t^{0.25}$. Similar conclusions have been drawn in the case of $Au/TiO_2(110)$.[82]

B. Low temperature deposit and the families of $(111)_{Pt}/(001)_{MgO}$ epitaxies

This section presents *ex situ* GIXS experiments on a 3.5 nm thick Pt film (S1-98) deposited at 800 K without further annealing (Table I). In agreement with similar experiments,[31,32,34] the $\Theta/2\Theta$ scan perpendicular to the surface [Fig. 6(a)] shows dominant $(111)_{Pt}\|(001)_{MgO}$ epitaxial orientations, the rationale of which being the minimization of the surface energy of the film. Evidences for the $(001)_{Pt}\|(001)_{MgO}$ (roughly 2% of the material) and

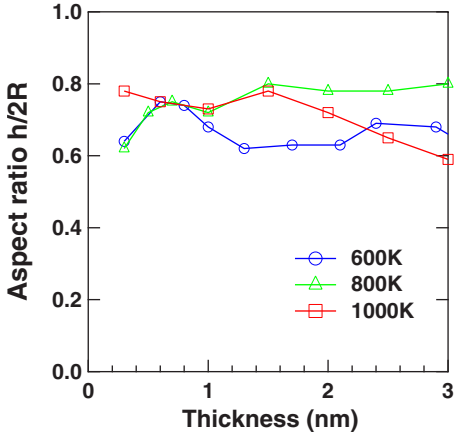

FIG. 5. (Color online) Evolution of the particle aspect ratio (height/diameter) for the three growth temperatures: 600 K (circle), 800 K (triangle), and 1000 K (square).

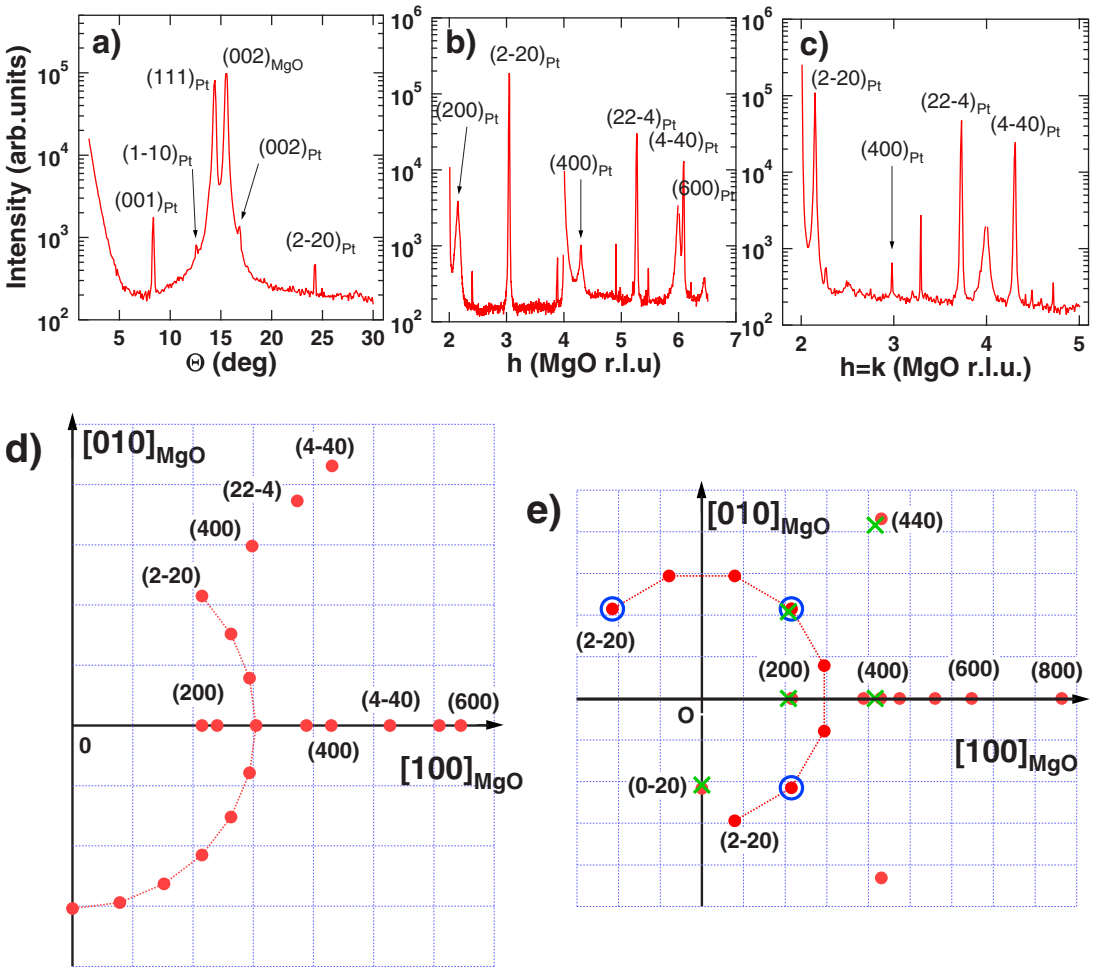

FIG. 6. (Color online) (a) $\theta/2\theta$ scan perpendicular to the sample surface (i.e., $\alpha_f=2\alpha_i$) obtained on a 3.5 nm thick sample deposited at 800 K (S1-98). [(b) and (c)] ($h00$) and ($hh0$) radial scans performed on the same sample. In these scans, the $(h00)_{Pt}$ peaks, with h even, correspond to the $(001)_{Pt}/(001)_{MgO}$ epitaxy, while the $(hh\bar{h}0)_{Pt}$ and $(hh2\bar{h})_{Pt}$ peaks correspond to the $(111)_{Pt}/(001)_{MgO}$ epitaxy. (d) Positions of all the peaks found experimentally in the reciprocal ($hk0$) plane (a) for the sample deposited at 800 K, which is mainly of (111) epitaxy, and (e) for all the remaining samples, which are mainly of (001) epitaxy. Only the Pt peaks have been reported (dots). The circle in (e) denotes peaks of $(2\bar{2}0)$ type, observed in the ω scan, while the crosses stand for the dislocation network.

$(1\bar{1}0)_{Pt}\|(001)_{MgO}$ ($\ll 1\%$) epitaxial orientations were also found by $\Theta/2\Theta$ scan [Fig. 6(a)] and radial scans [Figs. 6(b) and 6(c)]. The positions of all the in plane ($\ell \simeq 0$) $(111)_{Pt}$ and $(001)_{Pt}$ peaks observed herein have been gathered in Fig. 6(d) (sample S1-98) and Fig. 6(e) for all the other samples.

The orientations of the 800 K film S1-98 were investigated by means of a rocking ω scan of the $(2\bar{2}0)_{Pt}$ peak [Fig. 7(a)]. The $(2\bar{2}0)_{Pt}$ peaks related to the already reported $[1\bar{1}0](111)_{Pt}\|[110](001)_{MgO}$ orientation[30,32,34,35] are labeled "(i)" in Fig. 7(a). These peaks are expected every 30° because of the threefold symmetry of the epitaxial $(111)_{Pt}$ plane and the existence of four equivalent $\langle 110\rangle_{MgO}$ directions in the $(001)_{MgO}$ plane. In passing, the $[1\bar{1}0](111)_{Pt}\|[1\bar{1}0]\times(001)_{MgO}$ variant was also observed.[34] More interestingly, an orientation relationship $[1\bar{1}0](111)_{Pt}\|[100](001)_{MgO}$ was revealed by the appearance of $(2\bar{2}0)_{Pt}$ peaks with an offset of 15° as compared to $[1\bar{1}0](111)_{Pt}\|[110](001)_{MgO}$. These peaks are labeled "(ii)" in Fig. 7(a). According to integrated intensities, the $[1\bar{1}0]_{Pt}\|[110]_{MgO}$ and the $[1\bar{1}0]_{Pt}\|[100]_{MgO}$ represent 65% and 35% of the (111)-oriented Pt film, respectively. On the radial scans of Figs. 6(c) and 6(d), the $(hh\bar{h}0)_{Pt}$ and $(hh2\bar{h})_{Pt}$ peaks arise from the $[1\bar{1}0](111)_{Pt}\|[100]\times(001)_{MgO}$ interfaces. The $(h00)_{Pt}$ peaks with h even correspond to the $(001)[100]_{Pt}\|(001)[100]_{MgO}$ cube-on-cube epitaxy. It is worth noticing that the metal adlayer did not seem to be constrained since all the Pt reflections were bulklike. Representations in direct and reciprocal spaces of all epitaxies are given in Fig. 8.

The diffraction peaks labeled "(i)" in Fig. 7(a) ($[1\bar{1}0]\times(111)_{Pt}\|[110](001)_{MgO}$) exhibited satellites of lower intensity with well-defined offsets of ±2.4°, ±2.7°, ±3.6°, and ±5° [Fig. 7(b)] which, to our knowledge, have never been observed before. These satellites correspond to pure rotations since they were observed at the same disorientation angles at two different photon energies (11 and 18.5 keV). Such peaks correspond to Pt crystallites of given sizes rotated by a spe-

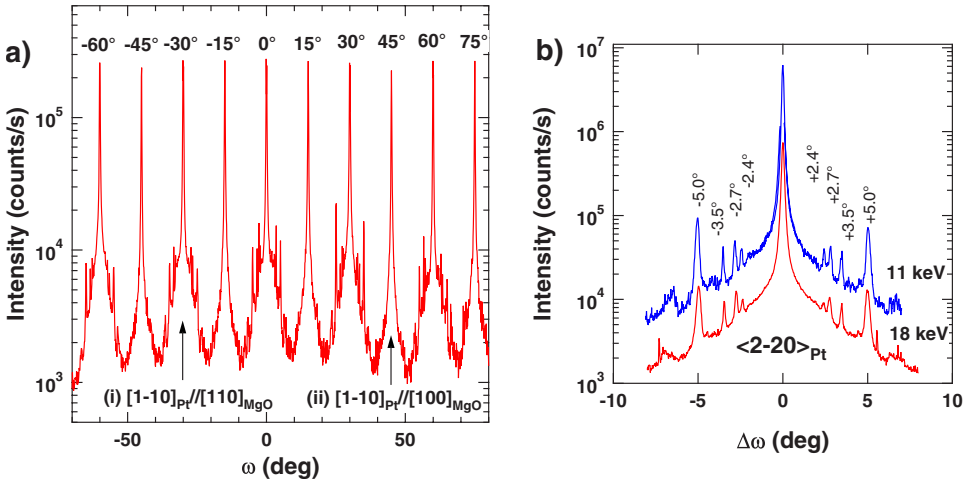

FIG. 7. (Color online) (a) A rocking ω scan of the $(2\bar{2}0)_{\mathrm{Pt}}$ peak, measured for the sample deposited at 800 K (S1-98). Peaks corresponding to the (i) $[1\bar{1}0]\times(111)_{\mathrm{Pt}}\|[110](001)_{\mathrm{MgO}}$ and (ii) $[1\bar{1}0](111)_{\mathrm{Pt}}\|[100](001)_{\mathrm{MgO}}$ epitaxies are repeated every 30°, respectively, with an offset of 15°. (b) A magnification of a peak of type (i) showing slightly rotated reflections. The scans acquired at two different photon energies are shown.

cific angle around the surface normal. The rotation might lower the interface energy, which is relatively high because of the large lattice mismatch at the $(111)_{\mathrm{Pt}}\|(001)_{\mathrm{MgO}}$ [Fig. 8(c)] interface. The in-plane coherent domain size d_ω was estimated by means of the Scherrer's formula

$$d_\omega = \frac{2\pi}{Q\Delta\omega(Q)}, \tag{1}$$

where Q is the wave vector transfer of the corresponding $(hk\ell)$ reflection and $\Delta\omega(Q)$ its FWHM. Because a small distribution of rotations around the average value is probable, this estimation can only yield a lower limit on the grain size. These sizes d_ω (as well as the relative abundance, as derived from integrated intensities) were estimated to 54 nm (92.8%), 73 nm (0.28%), 65 nm (0.71%), 97 nm (0.37%), and 34 nm (2.46%) for rotations of ±0°, ±2.4°, ±2.7°, ±3.6°, and ±5°, respectively. The sizes of rotated domains are smaller than that of the nonrotated ones, while the $[1\bar{1}0]\times(111)_{\mathrm{Pt}}\|[100](001)_{\mathrm{MgO}}$ epitaxial islands [labeled (ii)] have a smaller size of d_ω=33 nm.

Stacking faults and twin formation were evidenced by out-of-plane ℓ scans. Figure 9(a) shows out-of-plane $(h\bar{h}l)_{\mathrm{Pt}}$ measurements made on the sample S1-98 for $h_{\mathrm{Pt}}=\frac{2}{3},\frac{4}{3},2$. These coordinates are given in reciprocal lattice units of hexagonal Pt. Figure 9(b) gives a sketch of the positions of the diffraction peaks associated with the (111) epitaxy. Because of the *ABC* stacking in the fcc Pt, the $(2\bar{2}0)$ peak of the (111) epitaxy appears at $(2\bar{2}0)+(2/3)(1\bar{1}\bar{1})$. Additional peaks correspond to "twinned" Pt domains with a reverse fcc stacking, i.e., *ACB*, with a mirror plane at the fault location. Around the $(2\bar{2}0)$ Bragg peak, these "twin" peaks appear at $(2\bar{2}0)+(2/3)(\bar{1}11)$. The appearance of the $(111)_{\mathrm{Pt}}$ reflections at the expected bulk Pt position shows that, at this thickness, the metal layer is fully relaxed in the direction perpendicular to the substrate.

C. High temperature $(001)_{\mathrm{Pt}}/(001)_{\mathrm{MgO}}$ epitaxy: Strain evolution

This section deals with the relaxation mechanism of the stress arising from the lattice mismatch of −6.83% of Pt

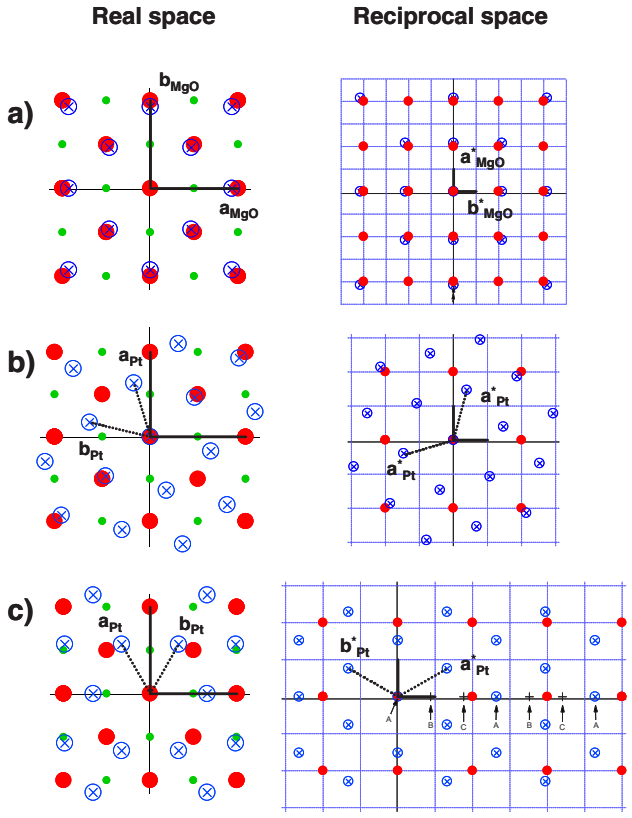

FIG. 8. (Color online) Rigid ball model of the epitaxial relationships at the Pt/MgO(001) interface in real (left panel) and reciprocal (right panel) spaces for the (a) $[100](001)_{\mathrm{Pt}}\|[100](001)_{\mathrm{MgO}}$, (b) $[1\bar{1}0](111)_{\mathrm{Pt}}\|[110](001)_{\mathrm{MgO}}$, and (c) $[1\bar{1}0](111)_{\mathrm{Pt}}\|[100](001)_{\mathrm{MgO}}$ epitaxial relationships. Pt atoms are represented by circled crosses, while Mg and O atoms are associated with full disks, respectively, small and large. On the right panel, MgO (Pt) reflections are shown as full circles (circled crosses), respectively. The direct and reciprocal MgO lattice vectors (a_{MgO}=4.2119 Å and a^*_{MgO}=1.4917 Å^{-1}) are represented by thick sticks. For $(001)_{\mathrm{Pt}}$ plane, a_{Pt}=3.9242 Å and a^*_{Pt}=1.6011 Å^{-1}, while the hexagonal lattice vectors for the $(111)_{\mathrm{Pt}}$ plane represented by dotted lines are given by $a_{\mathrm{Pt,h}}=\sqrt{2}/2a_{\mathrm{Pt}}$=2.7748 Å and $a^*_{\mathrm{Pt,h}}$=2.2643 Å^{-1}. In (c) (right), A, B, and C mark the positions corresponding to the first, second, and third (out-of-plane) layers of Pt atoms in the fcc stacking.

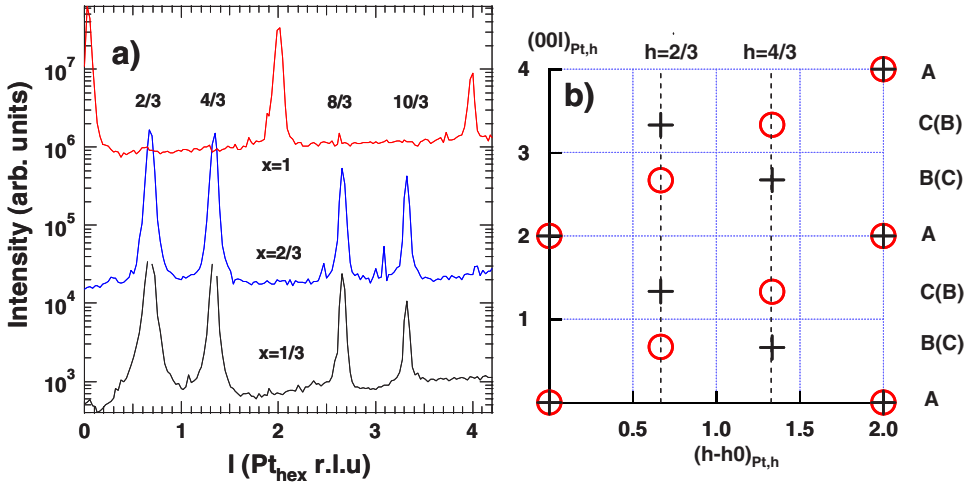

FIG. 9. (Color online) (a) Three out-of-plane ℓ scans made at $x\times(2\bar{2}\ell)_{\mathrm{Pt}}$ with $x=1/3,2/3,1$. The scans show the existence of twin fcc in the sample deposited at 800 K (S1-98). The upper scans have been shifted for clarity. (b) A schematic description of the reciprocal space in the $(h\bar{h}\ell)_{\mathrm{Pt,hex}}$ plane. Crosses denote the peaks arising from *ABC* stacking along the $(1\bar{1}1)$ direction, while circles denote the peaks arising from the $(\bar{1}11)$ direction. The two stacking variants are marked on the right scale. Note that reciprocal lattice units of the hexagonal Pt lattice have been used.

films with $[100](001)_{\mathrm{Pt}}\|[100](001)_{\mathrm{MgO}}$ epitaxy, such as those grown *in situ* at 1000 K or *ex situ* and then annealed at 1500–1600 K (Table I). On the 19.5 nm thick and annealed film (S2-98, Table I), the rocking ω scan around $(2\bar{2}0)_{\mathrm{Pt}}$ (Fig. 10) mostly detects this cube-on-cube epitaxy with only 3% of the film in the (111) orientation. This is quite similar to Pt/MgO(001) films *in situ* grown above 1000 K (Refs. 32 and 34) (see Fig. 11), which indicates that 1500–1600 K is a high enough annealing temperature to get Pt films close to equilibrium.

Lattice parameters were measured by *in situ* GIXS during the growth of Pt films at 1000 K, via the determination of the Pt Bragg peak positions by fitting the peak profiles with Lorentzians. At coverages between 0.1 and 6.5 nm, the cube-on-cube epitaxy was systematically evidenced by radial scans performed along the $(hh0.1)$ direction around $h=2$ [Fig. 11(a)] and along the $(h00.1)$, $(hh0.1)$, and $(h\bar{h}0.1)$ directions around $h=2,4$. Data showing a clear dependence of the Pt lattice parameter a_{Pt} on thickness are reported in Fig. 11(b). At low coverage (0.1–0.2 nm), the parameter $a_{\mathrm{Pt}}=0.393$ nm (as derived from the h values: $h\sim\pm2.15,\pm4.30$ MgO rlu) is close to that of bulk Pt [Fig. 11(b)]. Then, the Pt lattice parameter increases with coverage and reaches a maximum for a deposited thickness of 0.6 nm, where $a_{\mathrm{Pt}}=0.398$ nm ($h\pm2.12$ and $h\pm4.24$). At the same coverage, ℓ scans ($hh\ell$, where $h=1.08,2.15,4.30$) show a decrease of the out-of-plane Pt parameter with a value (0.388 nm) lower than the bulk value because of surface stress.[9] The deformation of the Pt unit cell thus happens at constant volume within 1%. At higher coverage, the 5.0 nm thick Pt film is almost completely relaxed, with a lattice parameter of 0.393 nm [Fig. 11(b)]. Therefore, at Pt coverages between 0.2 and 0.6 nm, the in-plane Pt parameter expands to reduce the film-substrate mismatch. It then progressively recovers the bulk values as the coverage increases. Owing to the bulk lattice mismatch (−6.83%), the introduction of the first dislocation at the interface should occur at a mean lateral island size of 6.2 nm. The comparison with the GISAXS size measurement allows us to point out [arrow in Fig. 11(b)] the correlation with the onset of the relaxation of the in-plane lattice Pt parameter. These evolutions of the strain of the Pt/MgO(001) clusters are similar to those observed for Ag/MgO(001),[8,15] but with a lack of pseudomorphic Pt.

In both radial and rocking scans, the diffraction peaks were observed to narrow and to increase in intensity as the deposition proceeds. The rocking width $\Delta\omega(Q)$ may originate from either the limited size $d_\omega=2\pi/\Delta Q_\omega$ of the Pt clusters, which results in a constant size broadening in the reciprocal space, or from the in-plane mosaic spread M.[9] For uncorrelated broadening, the peak width in reciprocal space is given by

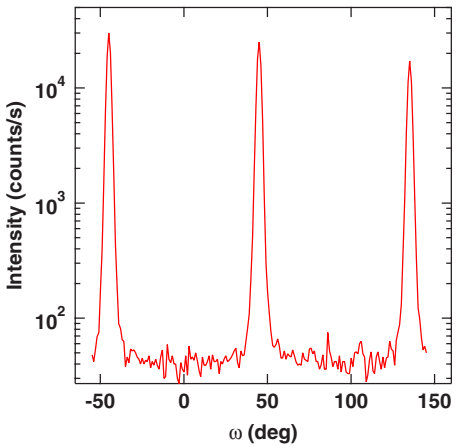

FIG. 10. (Color online) Rocking ω scan around the $(2\bar{2}0)_{\mathrm{Pt}}$ reflection for the sample S2-98 annealed at 1500 K. The fourfold symmetry compared to Fig. 7 confirms the cube-on-cube epitaxy.

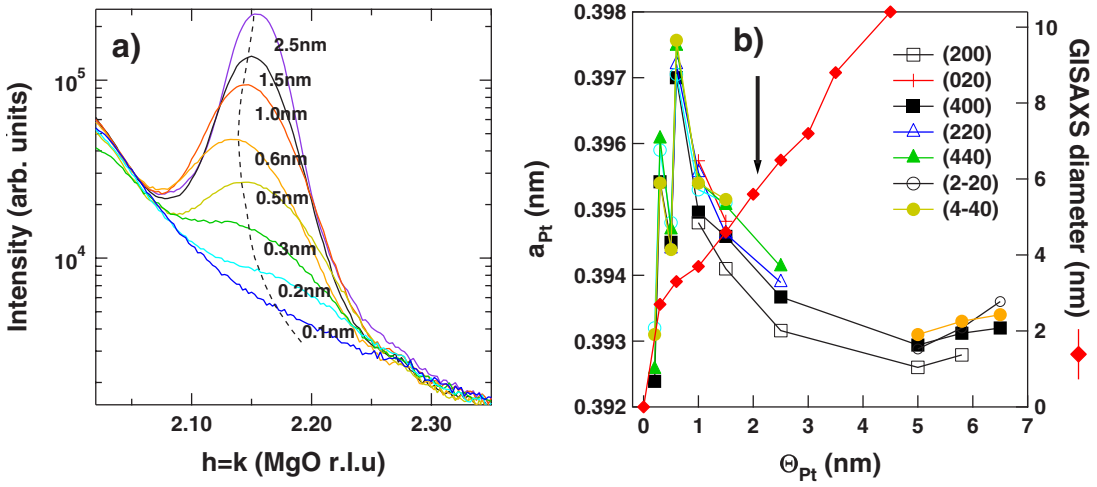

FIG. 11. (Color online) (a) Radial scans along the $(hh0.1)$ direction around the $(2\bar{2}0)_{\mathrm{Pt}}$ reflection as a function of the amount of deposited Pt at 1000 K (S1-99 and S2-99). The dotted line was added to guide the eyes. (b) Evolution with Pt thickness of the in-plane lattice parameter a_{Pt} as deduced from Lorentzian least-squares fits of $(h00.1)$, $(hh0.1)$, and $(h\bar{h}0.1)$ Pt peaks of various orders (left scale). The mean particle diameter extracted from the GISAXS analysis is given on the right scale. The arrow shows the onset of introduction of the first dislocation as deduced from the bulk lattice mismatch.

$$Q^2\Delta\omega^2(Q) = \Delta Q_\omega^2 + Q^2M^2. \tag{2}$$

The domain size $d_r = 2\pi/\Delta Q_r$ can also be determined by analyzing the FWHM of radial scans. The gradient of the crystallite lattice parameter $\Delta a/a$ also adds to the total peak width:

$$\Delta Q^2(Q) = \Delta Q_r^2 + \left(\frac{\Delta a}{a}\right)^2 Q^2. \tag{3}$$

The domain sizes d_ω and d_r, the mosaic spread M, and the gradient of lattice parameter $(\Delta a/a)$ are calculated from the FWHM of the peaks recorded by rocking and radial scans at various thicknesses for a growth temperature of 1000 K. Estimates of domain sizes derived from radial and rocking GIXS scans agree nicely within the experimental error bars and the two sets of values compare well with the lateral sizes determined by GISAXS as seen in Table III. Upon increasing the film thickness, the in-plane mosaic spread slightly increases (Table III). Notably, the decrease of the ratio $\Delta a/a$ indicates that the Pt grains become less strained as the coverage increases, which is consistent with the conclusion of the previous paragraph.

The epitaxial growth of a film (lattice parameter a_f) with a strong mismatch relative to a substrate (lattice parameter a_s) results in alternating zones of "good match" and "poor match" which form a network, often referred to as the coincidence site lattice (CSL),[83] with a period of $\Lambda = \frac{a_f a_s}{(a_f - a_s)}$. In most cases, this network corresponds to the existence of ordered misfit dislocations at the interface. This superperiodicity in the thin film yields satellite diffraction peaks in reciprocal space, around the Bragg peaks of the substrate and film, as has been evidence in the similar systems Ag/MgO(001) (Ref. 4) and Pd/MgO(001).[9] Such satellites are clearly visible along both $(h00)$ and $(hh0)$ radial directions around $h=2$ and 4 (Fig. 12) for sample S2-98. The $h=2.153$ and 4.30 peaks correspond to relaxed Pt, and the satellites are found around $h=2.075$ and 4.15. For a thick, continuous film in which the network is well ordered, some satellite peaks should be symmetry forbidden, according to the actual orientation and Burger's vector of the dislocations. At variance, for thinner films in the form of islands containing only few dislocations, all satellites are allowed.[8,9] Hence, if such satellites indicate that ordered misfit dislocations are present at the interface, the present data do not allow us to conclude on their type. The two possible types, oriented either along the $\langle 100\rangle$ or the $\langle 110\rangle$ directions, correspond, respectively, to bonding of the metal alternatively on top of oxygen and magnesium ions, or only on top of oxygens. Because of the much larger adsorption energy in this latter case, the dislocation network is most likely of the $\langle 110\rangle$ type, with $\frac{1}{2}[110]$ Burger's vector. Note that in-plane compressive strains in Pt/MgO film were reported earlier.[23,34] A transmission electron microscopy study of Pt/MgO(001) revealed a misfit dislocation network of an additional (020) Pt plane with a periodicity of 2.7 nm (14 Pt planes vs 13 MgO planes),[34] though the CSL orientation could not be determined.

IV. DISCUSSION

The present experiments demonstrate the existence of various $(111)_{\mathrm{Pt}}\|(001)_{\mathrm{MgO}}$ epitaxies and a strain relief mechanism of the $(001)_{\mathrm{Pt}}\|(001)_{\mathrm{MgO}}$ via the introduction of dislocations at the interface. The rationale of these is now discussed by calculating the equilibrium structures of platinum clusters supported on the MgO(001) surface.

A. Minimum energy clusters: (001) versus (111) epitaxy

To estimate the relative stability of supported metal particles of different sizes (defined by the number of atoms N)

TABLE III. The results of the analysis of the widths of the in-plane diffraction peaks measured on the *in situ* deposited samples at 1000 K. This table gives the Pt film thickness t, the investigated peak $(hk\ell)$, its full width at half maximum (FWHM) ($\Delta\omega$ or ΔQ, respectively, for a rocking or radial scan), and the calculated in-plane domain size (d_ω and d_r). The island diameter simulated from the GISAXS patterns d_s (see Sec. III) is also included. Moreover, the mosaic spread M and the gradient of lattice parameter $\Delta a/a$ calculated from the rocking and radial scans, respectively, are also presented.

t (nm)	$(hk\ell)$	$\Delta\omega$ (deg)	d_ω (nm)	M (deg)	ΔQ_r (rlu)	d_r (nm)	$\Delta a/a$	d_s (nm)
0.5	$(2\bar{2}0)/(4\bar{4}0)$				0.108/0.131	4.2	0.022	
1.0	(200)/(400)	2.49/1.72	4.7	1.10	0.089/0.107	5.2	0.028	~4.5
	(220)/(440)	2.01/1.39	5.1	1.08	0.082/0.094	5.4	0.014	
	$(2\bar{2}0)/(4\bar{4}0)$			1.10	0.080/0.100	5.9	0.020	
1.5	(200)/(400)				0.070/0.084	6.5	0.02	~5.4
	(220)/(440)				0.060/0.069	7.4	0.01	
	$(2\bar{2}0)/(4\bar{4}0)$				0.057/0.710	8.0	0.013	
2.5	(200)/(400)				0.058/0.066	7.7	0.014	~9.2
	(220)/(440)				0.049/0.050	8.9	0.005	
	$(2\bar{2}0)/(4\bar{4}0)$				0.057/0.710	8.0	0.013	
5.0	(200)/(400)	2.01/1.43	8.3	1.25	0.062/0.079	7.8	0.018	
	$(2\bar{2}0)/(4\bar{4}0)$	1.63/1.36	8.3	1.25			0.012	
5.8	(200)/(400)	1.946/1.22	8.5	1.25				
	$(2\bar{2}0)/(4\bar{4}0)$	1.61/1.35	8.4	1.26				

and to be able to identify the most stable clusters, we systematically used the average specific surface energy. This energy can be estimated from the total energy $E(N)$ of a cluster of size N and from the Pt bulk cohesive energy ϵ_B by $\Delta(N)=[E(N)-N\epsilon_B]N^{-2/3}$ (Refs. 19, 61, and 84). In analogy to the liquid drop model $[E(N)\sim N\epsilon_B+N^{2/3}\epsilon_S]$, it corresponds to the average surface energy ϵ_S and enables the elimination of the bulk contribution, which otherwise drives the behavior of $E(N)$. In the case of Pd/MgO(001), we have shown that the minima of $\Delta(N)$ can be associated with magic clusters of enhanced stability.[67] In the following, we focus on clusters corresponding to local minima of $\Delta(N)$ only.

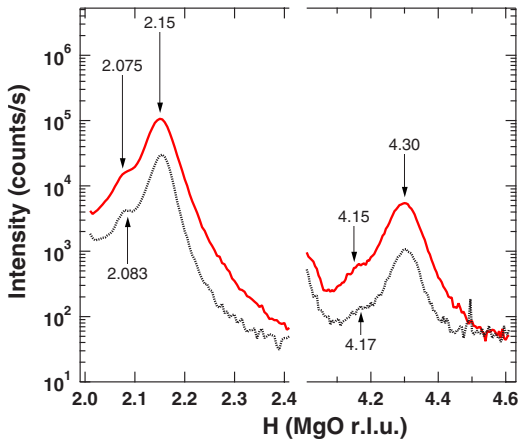

FIG. 12. (Color online) Radial scans around $(h00.05)$ (full line) and $(hh0.05)$ (dotted line) of a 19.5 nm thick Pt film deposited at room temperature and annealed at 1500 K. The intermediate peak is likely associated with a network of interfacial misfit dislocations.

In the case of the Pt(111) epitaxy (Fig. 13), $\Delta(N)$ decreases rapidly at the smallest cluster size and then reaches a practically constant value. This decrease is driven mainly by the reduction of the ratio of undercoordinated Pt atoms in the cluster. The latter is also responsible for the calculated monotonic increase of the average Pt-Pt distances at the interface (Fig. 13). For the (111) epitaxy, the coincidence of Pt and O lattices is relatively bad and, except for the smallest clusters, it changes only little as a function of cluster size. As a consequence, the adhesion energy is weak ($W_{(111)}\sim 0.25$ eV per interface Pt atom or 0.61 J/m^2) and remains practically constant along the series, so does the interface distance, which converges rapidly to $d_{int}=2.75$ Å. Influence of the substrate on the deposited cluster can be found in a weak oscillation of $\Delta(N)$, correlated to the introduction of subsequent zones of enhanced Pt-O coincidence at the interface (see the corresponding pressure maps in Fig. 13). Its effect on the cluster shape or atomic structure is practically negligible. In agreement with the absence of an experimental evidence on the substrate-induced strain, we find that beyond the smallest clusters, the average Pt-Pt distances recover rapidly their bulk value.

Unlike the (111) ones, for small clusters in Pt(001) epitaxy (Fig. 14), the calculated $\Delta(N)$ increases progressively until the regime of small oscillations around a practically constant value is reached. This behavior is driven by the

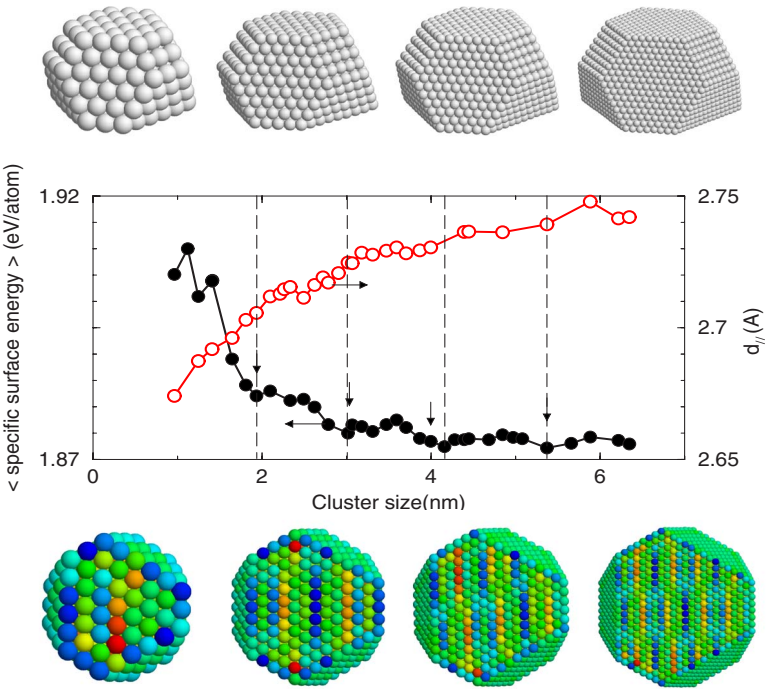

FIG. 13. (Color online) Behavior of the selected characteristics of Pt clusters in $(111)_{Pt}\|(001)_{MgO}$ epitaxy as a function of cluster size: average specific surface energy and average Pt-Pt distance in the interface layer $d_{\|}$. Top panel presents four clusters of sizes indicated by arrows. Bottom panel depicts the corresponding maps of pressure in the interfacial metal layer (red, compression; blue, tension).

weakening of the average Pt-MgO interaction due to the deteriorating coincidence at the interface as the cluster size increases. The related progressive reduction of the adhesion energy overrides other contributions to $\Delta(N)$, including that due to changes of the ratio of undercoordinated atoms. It is correlated with the behavior of the average Pt-Pt distance in the interfacial layer $d_{\|}$ as a function of cluster size. Whereas for small clusters $d_{\|}$ increases beyond the Pt bulk value, it undergoes a sudden contraction when the interface misfit dislocation appears. A similar change in Ag-Ag distance observed for Ag(001)/MgO(001) could be associated[15] with the appearance of dislocations.[8] Such behavior, typical of the (001) epitaxy, was already predicted for MgO(001)-supported Pd and Ni clusters.[19,61] In the present case, the abrupt reduction of $d_{\|}$ can be directly correlated with the experimental results [Fig. 11(b)] where indeed, after an initial progressive increase of the measured a_{Pt}, its rapid decrease occurs starting at $t \sim 1$ nm. Although we did not consider clusters large enough as to observe a full network of $\langle 110 \rangle$ interfacial misfit dislocations, the size at which the first one appears enables a rough estimation of the corresponding period to about 4.1 nm. This estimation agrees fairly well with the experimental data. In Pt(001) epitaxy, the coincidence of Pt and oxygen adsorption sites is relatively good,

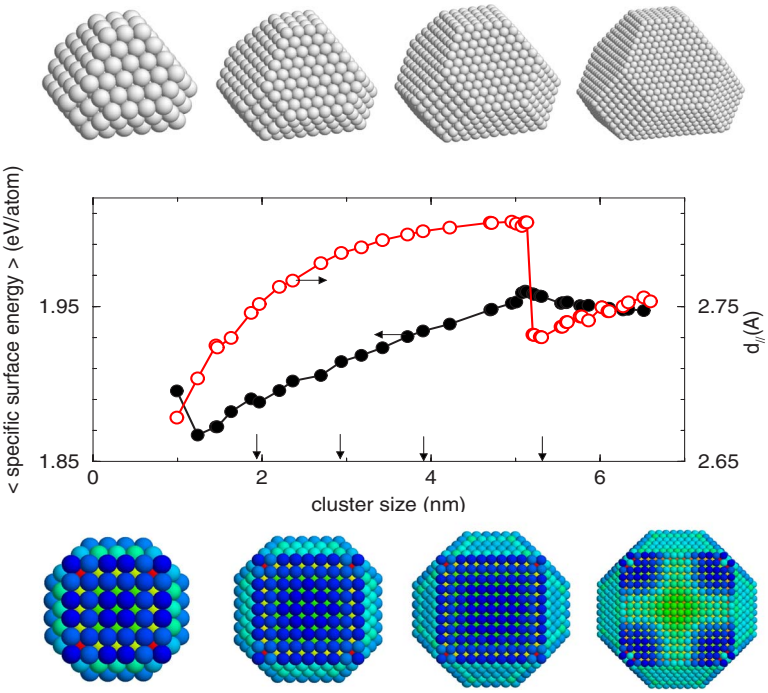

FIG. 14. (Color online) Behavior of the selected characteristics of Pt clusters in $(100)_{Pt}\|(001)_{MgO}$ epitaxy as function of cluster size: average specific surface energy and average Pt-Pt distance in the interface layer $d_{\|}$. Top panel presents four clusters of sizes indicated by arrows. Bottom panel depicts the corresponding maps of pressure in the interfacial metal layer (red, compression; blue, tension).

but it reduces considerably as the cluster size increases (see the corresponding pressure maps in Fig. 14). As a consequence, the adhesion is somewhat stronger, $W_{(001)} \rightarrow 0.30$ eV per interface Pt atom (0.64 J/m^2), and the average interface distance is systematically smaller ($d_{int} \rightarrow 2.64$ Å) if compared to the case of the (111) epitaxy.

As can be expected from $W_{(001)/(111)} < \sigma_{(001)/(111)}$ for both epitaxies, the clusters expose re-entering angles at the interface. Calculated cluster aspect ratio (as deduced from diagonal elements of the inertia tensor) H/d is equal to 0.7 for the (111) epitaxy and to 0.75 for the larger clusters in the (001) one. Both these values approach closely the simple Wulff-Kaishew estimation $H/d = 1 - W/2\sigma$. Additionally, $W_{(001)}/\sigma_{(001)} < W_{(111)}/\sigma_{(111)}$ results in a somewhat smaller H/d for the (111) epitaxy. Although this result agrees fairly well with the experimental estimation of ~0.7, we expect that a more precise computational estimation of the Pt surface energies would produce a somewhat larger H/d. As a rough guideline, a simple Wulff-Kaishew construction based on the experimental value of the surface energy yields $H/d \sim 0.9$. This suggests a possible underestimation of the equilibrium aspect ratio by the present experiment.

A comparison of the average specific surface energy $\Delta(N)$ calculated for clusters in the two epitaxies (Figs. 13 and 14) allows an analysis of their relative stability. We find that, beyond the smallest particles, $\Delta(N)$ calculated for clusters in the (111) epitaxy is systematically somewhat smaller, thus indicating an energetic preference for this latter epitaxy. While this trend may seem to contradict the conclusion obtained from the experimental results, it is worth noting that the computational results correspond to 0 K structures and that a possibility of a solid-solid cluster shape (and/or epitaxy) transition with increasing temperature cannot be excluded (see Ref. 66). On the other hand, in what concerns the computational findings, two sources of potential errors can be pointed out. First, the energetic model is not accurate enough. Indeed, the average surface energies calculated for the two families of clusters differ by less than 0.05 J/m^2 only. Such a small error can be attributed to the joined effect of the underestimated anisotropy factor $\sigma_{001}/\sigma_{111}$ [reduced energetic preference for the (111) facets] and of the underestimated aspect ratio H/d [ratio of total surface of the (001) and of the (111) facets is different from the experimental one]. Second, the "truncated Wulff polyhedron" hypothesis imposed on the shape of simulated clusters is too rigid. Dynamical calculations are scheduled in order to tackle this problem and to quantify the difference between equilibrium and growth cluster shapes.

B. Angular characteristics of the (111) epitaxy

In the following, we focus on the Pt(111) epitaxy and analyze the alternative orientations ω of clusters and substrate lattices. To this goal, we have evaluated the relation between cluster energy and the lattice orientation $E(\omega)$ by a partial relaxation of clusters deposited at different initial ω rotations. While for the smallest particles, the complete clusters were explicitly treated, for larger ones ($d > 2$ nm), truncated clusters composed of only six Pt layers were used in the calculation. Additionally, for cluster sizes beyond these reported above $d > 6$ nm, we have constructed the metal deposits by imposing the truncated triangular shape of the cluster base, as extrapolated from the fully optimized results on smaller particles. Finally, for the biggest clusters ($d > 12$ nm), we have fully neglected the atomic relaxation of the Pt deposit. Figure 15(a) shows a set of typical $E(\omega)$ profiles obtained for clusters of different sizes. As expected from symmetry considerations and in agreement with the experimental findings, the computed profiles are systematically characterized by the 30° periodicity and an inversion symmetry around $\omega = 15°$. In general, each of them possesses

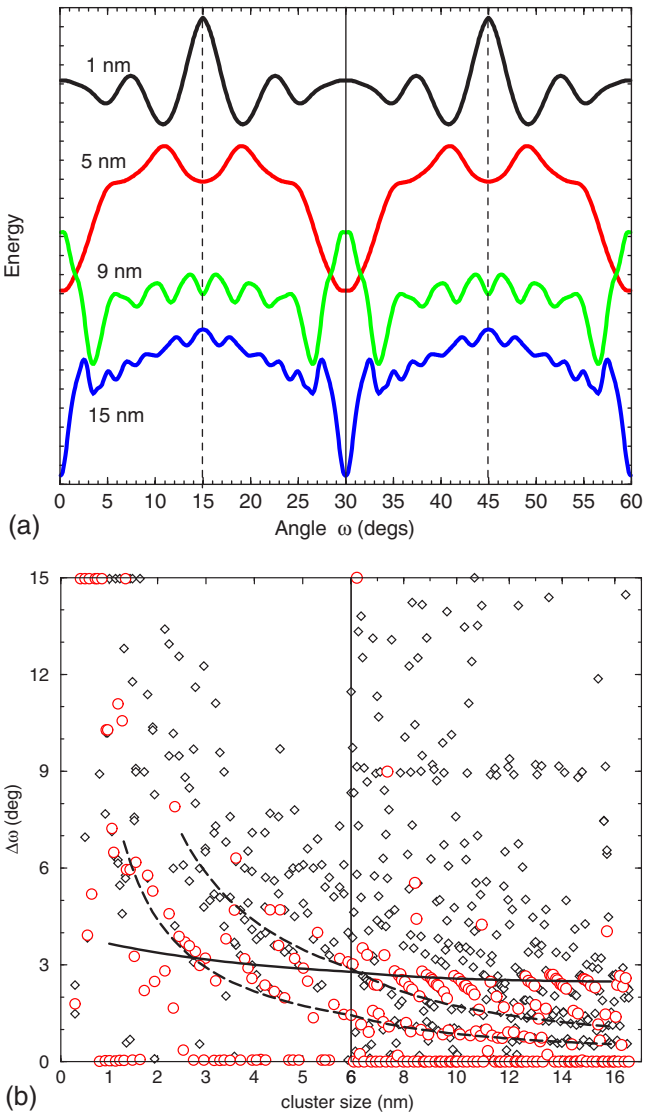

FIG. 15. (Color online) (a) Typical energy versus orientation angle $E(\omega)$ profiles for Pt(111) clusters deposited on the MgO(001) surface (top to bottom: sizes of 1, 5, 9, and 15 nm). Profiles were shifted on the energy scale so as to enter the graph. (b) Disorientation angles as a function of cluster sizes. For each size, the red circle represents the most stable orientation (global minimum). Black squares depict other most favorable local minima. The $\omega = 0°$ corresponds to $[1\bar{1}0]_{Pt} \| [110]_{MgO}$ orientation (see Figs. 7 and 8). Full and dashed lines are drawn as a guide for the eyes.

several distinct local minima, separated by energy barriers. In particular, for profiles depicted in Fig. 15(a), the most energetically favored solutions correspond to the high symmetry $\omega=0°$ ($[1\bar{1}0]_{Pt}\|[110]_{MgO}$) or 15° ($[1\bar{1}0]_{Pt}\|[100]_{MgO}$) orientations, but, especially for smaller sizes, other orientations are also present.

To get a complete view on the possible cluster orientations, in Fig. 15(b), we have represented a mapping of global and principal local minima of the $E(\omega)$ profiles as a function of cluster size. We notice a good coherence between results in regions treated on the different levels of approximation. For the smallest clusters ($d<2$ nm), beside the two high symmetry orientations $\omega=0°$ and 15°, we find also a large variety of possible stable (global minima) orientation angles located in the whole range $0° \leqslant \omega \leqslant 15°$. As the cluster size increases ($2<d<10$ nm), the region of energetically privileged orientations reduces progressively in favor of small angles. For larger clusters ($d>10$ nm), the global minima of $E(\omega)$ are located principally in three zones: (A) corresponds to the symmetric, zero degree orientation ($[1\bar{1}0]_{Pt}\|[110]_{MgO}$), (B) is a relatively narrow stripe of angles within the range $2° < \omega < 3°$, and (C) includes families of angles in the direct vicinity of the zero degree orientation ($\omega \sim 1°$).

In our model, the stabilization of a transition-metal/MgO(100) interface is driven principally by the coincidence of metal atoms with oxygen adsorption sites.[19] Compared to the $(001)_{Pt}/(001)_{MgO}$ epitaxy, the different symmetry of the coinciding lattices in the $(111)_{Pt}/(001)_{MgO}$ case reduces the size and proportion of the zones of good match, leading to a weaker interface adhesion and to a possibility of misorientations between the two lattices. For this epitaxy, the $\omega=0°$ orientation [zone (A)], which corresponds to an alignment of dense Pt rows with rows of substrate oxygen [see Fig. 8(c)], constitutes systematically a case of an enhanced stability driven by a particularly small (energetically unfavorable) Pt-Mg overlap. Beyond this particular case, while a small-period coincidence lattice can be obtained for $[1\bar{1}0]_{Pt}\|[9\bar{2}0]_{MgO}$ alignment [$\omega=2.47°$, zone (B)], lattices with a larger period and ω suffer from the unfavorable contribution due to noncoinciding Pt atoms, which systematically shifts the corresponding local minima of $E(\omega)$ toward higher energies.

While coincidence of infinite lattices accounts for $\omega=0°$ and $\omega=2.47°$ orientations, finite-size effects are visible in Fig. 15(b) already for the largest considered clusters ($d>10$ nm). On the one hand, size dependence of orientations in zone (C) is not related to changes of the interface misfit, the calculations for larger cluster being performed with fixed lattice parameters. The progressive decrease of the orientation angle can be rather associated with a succession of $[1\bar{1}0]_{Pt}\|[n\overline{(n-k)}0]_{MgO}$ alignments [for large n and small k, $\omega \rightarrow \arcsin(k/2n) \sim \arcsin(ka_s/2\sqrt{2}d)$, where d is the particle diameter, $n=1,2,3,\ldots$, and $k=1,3,5,\ldots$]. Close to $\omega=0°$, these orientations suffer from a small Pt-Mg overlap and benefit from the Pt-O coincidence of Pt atoms at the cluster edges. On the other hand, the size-dependent coincidence of Pt atoms at the cluster edges is also responsible for the stripelike structuration of zone (B) ($\omega=2.47°$) as a function of cluster size.

The above rigid-lattice arguments can also explain the major features in the preferential epitaxy orientations of smaller clusters, as exemplified with solid and dashed lines in Fig. 15(b), where additionally the reduction of the average Pt-Pt distances (from Fig. 13) has been included. For these particles, two additional effects need to be taken into account. On one hand, the contribution due to low-coordinated atoms at the cluster edges (which interact stronger with the MgO substrate) increases. On the other hand, small clusters and particularly their edges distort more easily. These two effects are at the origin of a variety of additional coincidence structures, beyond a simple extrapolation from these larger clusters. In particular, larger angles, including $\omega=15°$, appear as the most stable solutions for certain smaller Pt clusters.

The computational results show a good qualitative agreement with the experimental findings. They reveal a strong energetic preference for $\omega=0°$ epitaxy for larger clusters ($d \geqslant 10$ nm) and point out the existence of possible small-angle misorientations. On the contrary, the stability of $\omega=15°$ epitaxy is limited to smaller clusters only and no stable misorientations exist. Moreover, while the essential features of the orientation spectrum can be explained by coincidences of rigid Pt and O lattices, the Pt-Mg overlap cancels the stabilizing effect of Pt-O interaction and efficiently reduces the stability of most of disoriented structures. At this point, it is important to remember that the clusters observed experimentally do not represent the thermodynamic equilibrium and that the distribution of their shapes, sizes, and orientations with respect to the substrate may be, to some extent, driven by the growth mode and conditions. These kinetic effects could explain the presence of larger ($\omega=3.6°, 5°$) misorientations beyond the smallest cluster sizes, or the somewhat extended stability of the $\omega=15°$ epitaxy. A more precise analysis thus requires taking these factors into account in the simulations and goes beyond the scope of the current study.

C. Comparison with the Pd/MgO(001), Ag/MgO(001), and Ni/MgO(001) interfaces

The structure and morphology of growing Ag,[8] Pd,[9] Ni,[85] and Pt (this work) on MgO(001) can be compared. In all four cases, the metal has fcc structure and the epitaxy is cube-on-cube at the investigated temperature. The misfit at these interfaces increases from −3.00% for Ag, −6.83% for Pt, −7.64% for Pd, and −16.4% for Ni. According to theoretical calculations, the metal-oxide bond varies significantly in the same order. Silver is physisorbed (0.1–0.3 eV/atom), while Pd (0.65–0.8 eV/bond) and Ni (0.88–1.24 eV/atom) are more strongly bonded. Values between 1.36 and 2.35 eV have been obtained for the adsorption of one Pt atom on oxygen sites of MgO(001) surfaces.[11,37,65] For Ag, Pt, and Pd thick films, the lattice parameter misfit was found to relax via a network of interfacial misfit dislocations. The relaxation at the Ni/MgO(001) interface was instead found to occur by the growth of Ni(110)‖MgO(001) grains in addition to the cube-on-cube epitaxy.[85]

The metal-MgO distance, 0.252 nm for Ag,[6,8] 0.222 nm for Pd,[9] and 0.188 nm for Ni,[85] reflects the strength of the interfacial bond. For Pd and Ni, the average height of "on-site" metal saturates at 2–3 atomic layers. The larger misfit of Ni is then compensated by the stronger bonding. On the contrary, very little on-site metal atoms were found for Ag films. The structure and morphology at these metal/MgO interfaces seem to be more influenced by the strength of the bonding at the interface than by the lattice parameter misfit.

A very similar conclusion can be drawn from the recent computational comparative study on the equilibrium shape of Ni, Pd, and Pt clusters[61] and Ag thin films supported on the MgO(001) surface.[22] Indeed, regardless of the very different interface lattice mismatch in these systems, the calculated interface adhesion energy, which takes into account the contribution due to the misfit interface dislocations and a full relaxation of the metal deposit, decreases monotonically along the series Ni, Pd, Pt, and Ag. This trend reflects well the progressive weakening of the metal-MgO(001) bonding, as estimated from model *ab initio* calculations on pseudomorphic interfaces (no dislocations, partial relaxation of deposited metal). This weakening also drives the increase of the calculated interface metal-MgO distance along the series.

V. CONCLUSIONS

The growth of platinum on MgO(001) was analyzed in a combined experimental and theoretical study. Experiments were performed by grazing-incidence x-ray diffraction at small (GISAXS) and wide (GIXS) angles. The theory coupled *ab initio* calculations on model Pt/MgO(100) systems and large-scale simulations of supported Pt clusters using a coordination-dependent interaction potential. GISAXS data showed that clusters formed by Pt deposition have a nearly constant aspect ratio, while those grown at the highest temperature of 1000 K tend to facet. The particle size obeys a $\sim t^{0.5}$ power law assigned to dynamic coalescence.

The growth of the Pt film above 1000 K was found to lead to cube-on-cube epitaxy $[100](001)_{\mathrm{Pt}} \| [100](001)_{\mathrm{MgO}}$ alone as well as annealing of the Pt(111) film at 1500–1600 K. As the cluster size increases, the in-plane Pt-Pt distance increases above the bulk value (0.393 nm), passes through a maximum (0.398 nm) at $t=0.6$ nm, and then relaxes back to the bulk value when the interface misfit dislocation appears, a behavior already observed in the case of Ag/MgO(001) and predicted by theory to be typical for (001) epitaxy. The experimental observation of an array of dislocations arising from the large mismatch of −6.83% at the Pt/MgO(001) interface is supported by theory.

Below 1000 K, due to a minimization of the surface energy of the film, the $(111)_{\mathrm{Pt}} \| (001)_{\mathrm{MgO}}$ dominates. Beside the known $[1\bar{1}0](111)_{\mathrm{Pt}} \| [110](001)_{\mathrm{MgO}}$ epitaxy, another epitaxial orientation is revealed, namely, $[1\bar{1}0](111)_{\mathrm{Pt}} \| [100] \times (001)_{\mathrm{MgO}}$. Moreover, families of orientations slightly rotated relative to the former epitaxy were evidenced, but not around the latter. Calculations supported the observation and revealed that intermediate minima in energy occur close to the $[1\bar{1}0](111)_{\mathrm{Pt}} \| [110](001)_{\mathrm{MgO}}$ epitaxy at angles that depend on the size of the particles. The experimental and theoretical data reported herein are in overall agreement with results relative to Ni/, Pd/, and Ag/MgO(001) interfaces. The progressive weakening of the metal-MgO bonding over the Ni, Pd, Pt, and Ag series in this order explains the decrease in adhesion energy as well as the increase in the metal-MgO distance, which are observed and calculated through that series.

ACKNOWLEDGMENTS

We thank Marion Noblet-Ducruet for her great technical help during the experiments. J.O. thanks the support of Stiftelsen Bengt Lundqvist Minne, Sweden. This work also benefited from the financial support of ACI NanoTechnologie and ANR PNANO (DiNaMo and SIMINOX) from the French Ministry of Research. J.G. is thankful to Christine Mottet for fruitful discussions.

*Corresponding author. remi.lazzari@insp.jussieu.fr
†jacques.jupille@insp.jussieu.fr
‡jacek.goniakowski@insp.jussieu.fr
§grenaud@cea.fr

[1] C. Noguera, *Physics and Chemistry at Oxide Surfaces* (Cambridge University Press, Cambridge, 1995).
[2] A. Miyamoto, T. Hattori, and T. Inui, Appl. Surf. Sci. **60/61**, 660 (1992).
[3] C. T. Campbell, Surf. Sci. Rep. **27**, 1 (1997).
[4] G. Renaud, Surf. Sci. Rep. **32**, 1 (1998).
[5] C. Henry, Surf. Sci. Rep. **31**, 231 (1998).
[6] A. M. Flank, R. Delaunay, P. Lagarde, M. Pompa, and J. Jupille, Phys. Rev. B **53**, R1737 (1996).
[7] P. Guénard, G. Renaud, and B. Vilette, Physica B **221**, 205 (1996).
[8] O. Robach, G. Renaud, and A. Barbier, Phys. Rev. B **60**, 5858 (1999).
[9] G. Renaud, A. Barbier, and O. Robach, Phys. Rev. B **60**, 5872 (1999).
[10] A. Ferrari and G. Pacchioni, J. Phys. Chem. **100**, 9032 (1996).
[11] I. Yudanov, G. Pacchioni, K. Neyman, and N. Rösh, J. Phys. Chem. B **101**, 2786 (1997).
[12] J. Goniakowski, Phys. Rev. B **57**, 1935 (1998).
[13] J. C. Sánchez-López, A. R. González-Elipe, and A. Fernández, J. Mater. Res. **13**, 703 (1998).
[14] J. Goniakowski, Phys. Rev. B **59**, 11047 (1999).
[15] A.-M. F. P. Lagarde, S. Colonna, and J. Jupille, Surf. Sci. **524**, 102 (2003).
[16] G. Renaud *et al.*, Science **300**, 1416 (2003).
[17] H. Graoui, S. Giorgio, and C. Henry, Surf. Sci. **417**, 350 (1998).
[18] H. Graoui, S. Giorgio, and C. Henry, Philos. Mag. B **81**, 1649 (2001).

[19] W. Vervisch, C. Mottet, and J. Goniakowski, Phys. Rev. B **65**, 245411 (2002).
[20] C. Revenant, F. Leroy, R. Lazzari, G. Renaud, and C. R. Henry, Phys. Rev. B **69**, 035411 (2004).
[21] F. Leroy, G. Renaud, A. Letoublon, R. Lazzari, C. Mottet, and J. Goniakowski, Phys. Rev. Lett. **95**, 185501 (2005).
[22] A. Ouahab, C. Mottet, and J. Goniakowski, Phys. Rev. B **72**, 035421 (2005).
[23] J. L. Menéndez, P. Caro, and A. Cebollada, J. Cryst. Growth **192**, 164 (1998).
[24] M. Morcrette, A. Guitierrez-Llorente, W. Seller, J. P. A. Laurent, and P. Barboux, Appl. Surf. Sci. **60/61**, 660 (1992).
[25] R. Davis and E. Derouane, Nature (London) **349**, 313 (1991).
[26] M. Aramendía, J. Benítez, V. Borau, C. Jiménez, J. Marinas, J. Porras, J. Ruiz, and F. Urbano, Colloids Surf., A **225**, 137 (2003).
[27] A. Hinz, P. Larsson, B. Skårman, and A. Andersson, Appl. Catal., B **34**, 161 (2001).
[28] J. F. M. Cillessen, R. M. Wolf, and D. M. de Leeuw, Thin Solid Films **226**, 53 (1992).
[29] Y. Takai and M. Sato, Supercond. Sci. Technol. **12**, 486 (1999).
[30] J. Narayan, P. Tiwari, K. Jagannadham, and O. W. Holland, Appl. Phys. Lett. **64**, 2093 (1994).
[31] P. McIntyre, C. Maggiore, and M. Natasi, Acta Mater. **45**, 869 (1997).
[32] P. C. McIntyre, C. J. Maggiore, and M. Natasi, Acta Mater. **45**, 879 (1997).
[33] R. Farrow, D. Weller, R. Marks, M. Toney, A. Cebollada, and G. Harp, J. Appl. Phys. **79**, 5967 (1996).
[34] C. Gatel, P. Baules, and E. Snoeck, J. Cryst. Growth **252**, 424 (2003).
[35] B. M. Lairson, M. R. Visokay, R. Sinclair, S. Hagstrom, and B. M. Clemens, Appl. Phys. Lett. **61**, 1390 (1992).
[36] P. Andreazza, C. Andreazza-Vignolle, J. Rozenbaum, A.-L. Thomann, and P. Brault, Surf. Coat. Technol. **151**, 122 (2002).
[37] H. Grönbeck and P. Broqvist, J. Chem. Phys. **119**, 3896 (2003).
[38] Y. Yoneda, K. Sakaue, and H. Terauchi, J. Phys.: Condens. Matter **12**, 8523 (2000).
[39] K. Zhao and H. K. Wong, J. Cryst. Growth **256**, 283 (2003).
[40] H. Fecht and H. Gleiter, Acta Metall. **33**, 557 (1985).
[41] H. Fecht, Acta Metall. **36**, 689 (1988).
[42] L. Vitos, A. Ruban, H. Skriver, and J. Kollár, Surf. Sci. **411**, 186 (1998).
[43] A. Turos, O. Meyer, and H. Matzke, Appl. Phys. Lett. **38**, 910 (1981).
[44] J. R. Levine, J. B. Cohen, Y. W. Chung, and P. Georgopoulos, J. Appl. Crystallogr. **22**, 528 (1989).
[45] I. K. Robinson and D. J. Tweet, Rep. Prog. Phys. **55**, 599 (1992).
[46] http://www.esrf.fr/UsersAndScience/Experiments/CRG/BM32/.
[47] R. Baudoing-Savois, M. De Santis, M. Saint-Lager, O. Dolle, P. Geaymond, P. Taunier, P. Jeantet, J. Roux, G. Renaud, and A. Barbier, Nucl. Instrum. Methods Phys. Res. B **149**, 213 (1999).
[48] G. Renaud, M. Ducruet, O. Ulrich, and R. Lazzari, Nucl. Instrum. Methods Phys. Res. B **222**, 667 (2004).
[49] L. B. N. Laboratory, Center for X-ray Optics, http://www-cxro.lbl.gov/.
[50] O. Robach, G. Renaud, and A. Barbier, Surf. Sci. **401**, 227 (1998).
[51] F. Ducastelle, J. Phys. (Paris) **31**, 1055 (1970).
[52] V. Rosato, M. Guillopé, and B. Legrand, Philos. Mag. A **59**, 321 (1989).
[53] C. Mottet, J. Goniakowski, F. Baletto, R. Ferrando, and G. Treglia, Phase Transitions **77**, 101 (2004).
[54] F. Montalenti, F. Baletto, and R. Ferrando, Surf. Sci. **454-456**, 575 (2000).
[55] E. Aprà, F. Baletto, R. Ferrando, and A. Fortunelli, Phys. Rev. Lett. **93**, 065502 (2004).
[56] S. Baud, C. Ramseyer, G. Bihlmayer, S. Blügel, C. Barreteau, M. C. Desjonquères, D. Spanjaard, and N. Bernstein, Phys. Rev. B **70**, 235423 (2004).
[57] W. Tyson and W. Miller, Surf. Sci. **62**, 267 (1977).
[58] A. R. Miedema, Philips Tech. Rev. **38**, 257 (1978).
[59] J. Goniakowski, C. Mottet, and C. Noguera, Phys. Status Solidi B **243**, 2516 (2006).
[60] S. Sao-Jaoa, S. Giorgio, C. Mottet, J. Goniakowski, and C. Henry, Surf. Sci. **600**, L86 (2006).
[61] C. Mottet and J. Goniakowski, J. Comput. Theor. Nanosci. **4**, 326 (2006).
[62] Y. Wang and J. P. Perdew, Phys. Rev. B **44**, 13298 (1991).
[63] G. Kresse and J. Hafner, Phys. Rev. B **47**, 558 (1993).
[64] http://www.crmcn.univ-mrs.fr/gModel/webparam.pdf
[65] A. Bogicevic and D. Jennison, Surf. Sci. **437**, L741 (1991).
[66] F. Baletto and R. Ferrando, Rev. Mod. Phys. **77**, 371 (2005).
[67] J. Goniakowski and C. Mottet, J. Cryst. Growth **275**, 29 (2005).
[68] C. Mottet and J. Goniakowski, Surf. Sci. **566-568**, 443 (2004).
[69] G. Wulff, Z. Kristallogr. **34**, 449 (1901).
[70] R. Kaischew, Bull. Acad. Sci. Bulg., Ser. Phys. **2**, 191 (1951).
[71] R. Lazzari, J. Appl. Crystallogr. **35**, 406 (2002).
[72] R. Lazzari, ISGISAXS can be downloaded with a user guide from http://www.esrf.fr/computing/scientific/joint_projects/IsGISAXS/isgisaxs.htm, 2002.
[73] M. Rauscher, R. Paniago, H. Metzger, Z. Kovats, H. D. Domke, J. Pfannes, J. Schulze, and I. Eisele, J. Appl. Phys. **86**, 6763 (1999).
[74] J. S. Pedersen, J. Appl. Crystallogr. **27**, 595 (1994).
[75] R. Hosemann and S. N. Bagchi, *Direct Analysis of Diffraction by Matter* (North-Holland, Amsterdam, 1962).
[76] J. L. Viovy, D. Beysens, and C. M. Knobler, Phys. Rev. A **37**, 4965 (1988).
[77] B. J. Briscoe and K. P. Galvin, Phys. Rev. A **43**, 1906 (1991).
[78] P. Meakin, Rep. Prog. Phys. **55**, 157 (1992).
[79] F. Family and P. Meakin, Phys. Rev. Lett. **61**, 428 (1988).
[80] F. Family and P. Meakin, Phys. Rev. A **40**, 3836 (1989).
[81] A. Steyer, P. Guenoun, D. Beysens, and C. M. Knobler, Phys. Rev. A **44**, 8271 (1991).
[82] R. Lazzari, G. Renaud, J. Jupille, and F. Leroy, Phys. Rev. B (to be published).
[83] H. Grimmer, W. Bollmann, and D. Warrington, Acta Crystallogr., Sect. A: Cryst. Phys., Diffr., Theor. Gen. Crystallogr. **30**, 197 (1974).
[84] W. Vervisch, C. Mottet, and J. Goniakowski, Eur. Phys. J. D **24**, 311 (2004).
[85] A. Barbier, G. Renaud, and O. Robach, J. Appl. Phys. **84**, 4259 (1998).